Int J Mech Mater Des (2021) 17:153–169
https://doi.org/10.1007/s10999-020-09521-x

The effect of negative Poisson's ratio on the low-velocity impact response of an auxetic nanocomposite laminate beam

Yin Fan · Yeqing Wang

Received: 16 May 2020 / Accepted: 27 August 2020 / Published online: 22 September 2020

Abstract In this paper, an investigation on the low-velocity impact (LVI) response of a shear deformable beam laminated by carbon nanotube reinforced composite (CNTRC) layers is performed. The composite beam is "auxetic" due to the negative out-of-plane Poisson's ratio (NPR) through special symmetric stacking sequences of layers that are designed based on the Classical Laminate Theory. To study the effect of the out-of-plane NPR on the LVI response of the composite beam, a newly defined Hertz model is developed. The motion equations of Kármán type for the CNTRC laminate beam are derived in the framework of the Reddy beam theory and solved by means of a two-step perturbation approach while the dynamic equation of the impactor is built on Newton's Law. Since temperature-dependent material properties of both carbon nanotube (CNT) and matrix are employed, the thermal influence on the LVI behavior is also investigated. Moreover, a piece-wise method is employed herein to investigate the effect of functionally graded (FG) patterns of the CNT reinforcements on the impact response. Numerical results elucidating the effects of temperature, FG distribution, and CNT volume fraction on the out-of-plane Poisson's ratio and impact response of the beam are obtained by using a Range–Kutta method and discussed in details.

Keywords Carbon nanotube reinforced composite · Auxetic laminated beam · Low-velocity impact · Negative Poisson's ratio · Temperature-dependent properties

1 Introduction

Nowadays, nanocomposites reinforced by carbon nanotubes (CNTs), which are perceived as the next generation advanced composite materials, have been widely studied all over the world due to their extraordinary mechanical properties and significant weight reduction capability when compared to traditional composite materials reinforced by fibers. Theoretically, the strength-to-weight ratio of CNTs can reach about 77,000 kN m kg^{-1} comparing to Kevlar fiber of 2500 kN m kg^{-1} (Takakura et al. 2019). The application of such lightweight materials on aerospace structures can translate directly to fuel saving and energy efficiency. In the design of composite structures, the performance of impact resistance is given priority to because the mechanical impact, such as the

Y. Fan
Marvin B. Dow Advanced Composites Institute, Mississippi State University, Starkville, MS 39759, USA

Y. Wang (✉)
Department of Mechanical and Aerospace Engineering, Syracuse University, 263 Link Hall, Syracuse, NY 13244, USA
e-mail: ywang261@syr.edu

low-velocity impact (LVI) caused by tool drop and high-velocity impact due to hail impact and bird strike, could seriously degrade the performance of the composite structure (Hill et al. 2012, 2013; Tan et al. 2012; Heydari-Meybodi et al. 2016). The impact damage tolerance is especially important for providing design guidance on determining the minimum allowable gauge thickness of composite structures (e.g., aircraft fuselage).

Negative Poisson's ratio (NPR), also known as "auxetic" (Evans et al. 1991), is an anomalous physical property (Fan et al. 2020) that conventional materials normally do not have. Theoretically, materials with NPR are expected to demonstrate a superior mechanical property to resist indentation by densifying in both the longitudinal and transverse directions subjected to impact (Mir et al. 2014). Figure 1 shows a comparison of the indentation responses between nonauxetic and auxetic materials. From the existing literature (Clarke et al. 1994; Harkati et al. 2007; Chen et al. 2013), the out-of-plane NPR is possible to be obtained through design and optimization of the stacking sequence for some fiber reinforced composite laminates. The key that enables the composite laminates to produce the out-of-plane NPR is the large anisotropicity of the single ply, as indicted by previous research (Harkati et al. 2007). In other words, the out-of-plane Poisson's ratio can be negative only when the difference between the Young's moduli of a single ply in the longitudinal direction and the in the transverse direction is large enough. One promising candidate of such composite to achieve the auxeticity (i.e., out-of-plane NPR) is the CNT/PmPV composite. Results from molecular dynamics (Han and Elliott 2007) show that the longitudinal modulus of CNT/PmPV with 14% volume fraction of CNT is about 52 times of the transverse modulus. In this study, this composite will be used to predict the out-of-plane NPR and investigate the NPR effect on the low-velocity impact response. Here, it should be mentioned that Shen and his co-authors (Shen et al. 2020a, b; Yang et al. 2020a, b) have already designed the auxeticity from carbon nanotube reinforced composite (CNTRC) laminates and analyzed the effect on vibration and flexural behaviors. However, the effect of the auxeticity on the LVI response of the composite, which is expected to greatly improve the impact resistance, has not yet been thoroughly studied.

To date, a number of theoretical and numerical investigations (Dai 2014; Wang et al. 2014; Jam and Kiani 2015; Malekzadeh and Dehbozorgi 2016; Ebrahimi and Habibi 2017; Salami 2017; Zarei et al. 2017; Bayat et al. 2018; Song et al. 2018; Fan and Wang 2017a, b) on the LVI of CNTRC structures have been conducted after the material properties of CNT (Han and Elliott 2007) and their corresponding micromechanical models (Shen 2009; Shen and Zhang 2010) were reported. In these studies, the emphasis is mainly placed on the functionally graded (FG) distributions of CNTs and their improvements in the material properties (Shen 2009; Kwon et al. 2011) and the impact behaviors. However, the impact models used in these studies have not accounted for the effect of the FG distribution and the out-of-plane NPR effect potentially produced from these auxetic CNT composites. Although the Hertz contact model was modified by Fan and Wang (2017a, b) by taking into account the FG influence, most studies still used the classical Hertz theory for isotropic bodies in contact which neglects the effect of out-of-plane Poisson's ratio.

To accurately analyze the LVI process, the contact law between the impactor and the object needs to be properly established. The first elastic contact model was proposed by Hertz in 1882. This model is generally used for both isotropic bodies in contact. Modification to this model is required if one wants to apply this model to the LVI analysis of composites, for

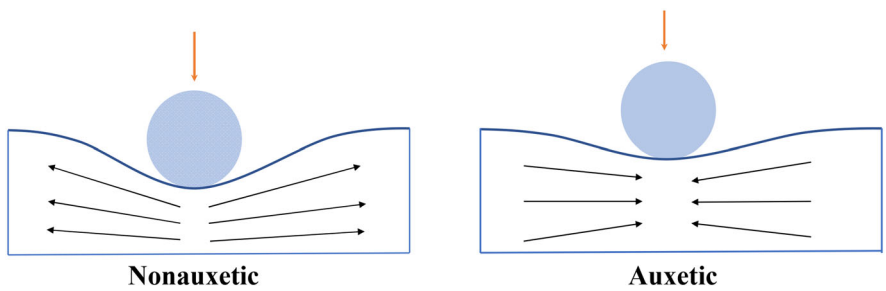

Fig. 1 A comparison of indentation response between nonauxetic and auxetic materials (Mir et al. 2014)

which the materials are normally treated as anisotropic materials (Mittal and Khalili 1994). Although the Hertz contact between two elastic anisotropic bodies (Sveklo 1974) was proposed in 1974, it has not been used much due to its mathematical complexity which involves the integration of imaginary numbers and difficulty in numerical implementations for engineering applications. Therefore, it seems extremely challenging to analyze the contact for composite materials. Fortunately, some special stacking sequences, such as symmetrical or anti-symmetrical layups, as well as some special structures (e.g., beam structure) would allow us to simplify the contact problem for composite materials, and thus, make the analysis of low-velocity impact practically more viable.

To authors' best knowledge, the present work is the first endeavor to analyze the effect of out-of-plane negative Poisson's ratio on LVI response of auxetic nanocomposite laminated structures. In this study, we focused on the CNTRC laminate which is designed to produce the effective out-of-plane NPR in either the direction of 13 or the direction of 23. Note that the Poisson's ratio in the direction of 13 is different from the value in the direction of 31 due to the anisotropicity of the Poisson's ratio in the 13 plane. In addition, the anisotropic NPR needs to be distinguished from the isotropic NPR (Hou et al. 2012), which denotes that the NPRs are same at two perpendicular directions in a plane. Materials with anisotropic NPRs would exhibit different auxetic behaviors if the loading is applied in different directions. On the contrary, materials with an isotropic NPR would show the same auxetic behavior as long as the loading is applied in the isotropic plane.

The auxetic CNTRC laminated structure considered in this paper is a Reddy beam (Heyliger and Reddy 1988), which allows us to simplify it into a one-dimensional (1D) structure in mechanics. For such 1D structure, the Hertz models for transversely isotropic materials (Turner 1979; Greszczuk 1982; Swanson 2005), which are much simpler than Hertz models for anisotropic materials in terms of mathematical calculation and numerical implementation, are adapted here in the current LVI analysis. In particular, the dynamic equation of the beam is built based on a higher order theory and von Kármán stress–strain relationship while the dynamic equation of the impactor is established on the foundation of Newton's second law of motion. The effective out-of-plane Poison's ratio is calculated through the **J** matrix derived based on the constitutive relation, using which, the stacking sequences for achieving the out-of-plane NPR effect can be obtained. Furthermore, the material properties of CNTRC are temperature-dependent. The motion equations of the impactor and the beam are solved by a fourth order Runge–Kutta method simultaneously. The parametric studies will illustrate the influences of CNT volume fraction, temperature, and FG pattern on both NPR and low-velocity impact behaviors of the nanocomposite beam.

2 Theoretical models

In the present study, we consider a laminated beam with length L, width b, and thickness h, which consists of 5 CNTRC plies. Each ply has a constant thickness h_p, and thus, the total thickness of the beam is $h = 5h_p$. The sphere-shape impactor has a mass m^i, an initial velocity $\bar{V}_0$, and a tip radius R^i. The impact location is at the center of the beam. The schematic of LVI on the beam is depicted in Fig. 2.

2.1 Modified contact model

The Hertz contact law is more accurate and complete than other contact theories in the case of LVI approximation (Rilo and Ferreira 2008; Abrate 2011). In the Hertzian theory, the contact force F_c can be expressed as:

$$F_c(t) = K_c[\delta(t)]^r, \tag{1}$$

where $\delta(t)$ denotes the indentation, whose definition is

$$\delta(t) = \bar{S}(t) - \bar{W}(t), \tag{2}$$

in which $\bar{S}(t)$ denotes the displacement of the impactor and $\bar{W}(t)$ represents the deflection of the plate at the impact location. For composite laminates, Sun and Chen (1985) identified a nonlinear contact relation based on the Hertz law in the loading phase for composite materials, where the exponent r in Eq. (1) can be determined empirically as 1.5. In the unloading phase, the contact force F_c can be written as

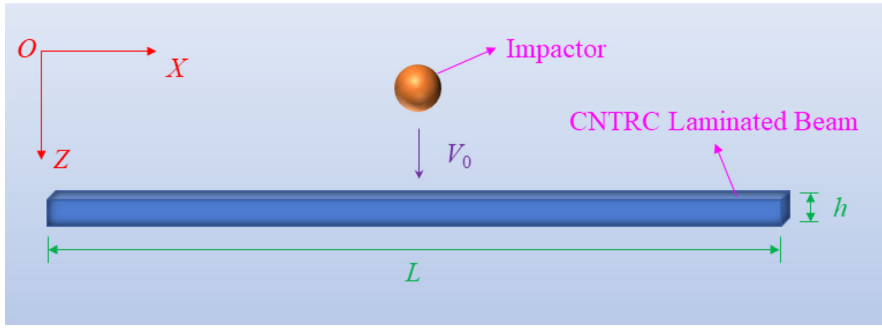

Fig. 2 Geometry and coordinate system of an auxetic CNTRC laminated beam

$$F_c(t) = F_{\max}\left[\frac{\delta(t)-\delta_0}{\delta_{\max}-\delta_0}\right]^s, \tag{3}$$

where $F_{\max}$ and $\delta_{\max}$ are the maximum contact force and indentation, respectively. The local indentation δ_0 equals to zero when $\delta_{\max}$ remains below a critical indentation during the loading phase. It was found that the exponent $s = 2.5$ provides a good fit to the experimental data when the diameter of the impactor is no larger than 1.27 cm (Sun and Chen 1985). In Eq. (1), K_c is defined as the contact stiffness and its expression is

$$K_c = \frac{4}{3}E^*\sqrt{R^i}, \tag{4}$$

where R^i is the radius of the impactor tip and E^* is the contact modulus, which is expressed by

$$\frac{1}{E^*} = \frac{1}{E_i^e} + \frac{1}{E_i^b}, \tag{5}$$

in which, E_i^e and E_i^b are effective contact moduli of the impactor and beam, respectively. The impactor made of metal is assumed to be isotropic, its effective contact modulus can be easily written as

$$\frac{1}{E_i^e} = \frac{1-v_i^2}{E_i}, \tag{6}$$

where E^i and v^i are the Young's modulus and Poisson's ratio of the impactor, respectively. Usually, for convenience, the expression of effective contact modulus for the composite beam can be written in a simple form by ignoring the effect of Poisson's ratio and written as

$$\frac{1}{E_i^b} = \frac{1}{E_{33}}, \tag{7}$$

in which E_{33} is the out-of-plane Young's modulus of the beam. However, Olsson et al. (2006) indicated that this tentative approximation of ignoring the Poisson's ratio effect might cause the underestimation of contact modulus by 10–20%. To include the effect of Poisson's ratio in the Hertz contact law, especially for out-of-plane, in this paper, we propose to modify the E_i^b originally suggested by Greszczuk (1982) for the transversely isotropic contact

$$\frac{1}{E_i^b} = \frac{\sqrt{\left(\sqrt{C_{11}^e C_{33}^e}+G_{31}^e\right)^2-\left(C_{13}^e+G_{31}^e\right)^2}}{2\sqrt{G_{13}^e/C_{11}^e}\left(C_{11}^e C_{33}^e - C_{13}^e C_{13}^e\right)}, \tag{8}$$

where C_{ij}^e and G_{ij}^e (i = 1, 3; j =1, 3) are effective material properties of the target beam and can be calculated by

$$\left(C_{ij}^e, G_{ij}^e\right) = \frac{1}{h}\int_{-h/2}^{h/2}\left(\bar{C}_{ij}, \bar{G}_{ij}\right)_k dZ, \tag{9}$$

in which $\bar{C}_{ij}$ and $\bar{G}_{ij}$ are material properties of the kth layer in a laminated beam and are functions of Poisson's ratios, which will be discussed in detail in the following section.

2.2 Out-of-plane Poisson's ratios

For the out-of-plane properties of a laminated CNTRC beam with N layers, we focus on the effective Poisson's ratios v_{13}^e and v_{23}^e, which are significantly affected by its stiffness. According to the Classical Laminate Theory (CLT), the out-of-plane effective Poisson's ratios are

$$v_{13}^{e} = -\frac{J_{31}}{J_{11}}, \tag{10a}$$

$$v_{23}^{e} = -\frac{J_{32}}{J_{22}}, \tag{10b}$$

in which J_{11}, J_{22}, and J_{33} are elements of the **J** matrix which can be written as

$$\mathbf{J} = \mathbf{A}^{-1} + \mathbf{A}^{-1}\mathbf{B}\left(\mathbf{D} - \mathbf{B}\mathbf{A}^{-1}\mathbf{B}\right)^{-1}\mathbf{B}\mathbf{A}^{-1}, \tag{11}$$

where **A**, **B**, and **D** are extension stiffness matrix, extension-bending coupling stiffness matrix, and bending stiffness matrix of the CNTRC laminate, respectively. The detailed derivation of **J** matrix is discussed in "Appendix A". The elements of the aforementioned stiffness matrixes **A**, **B**, and **D** can be defined as

$$\left(A_{ij}, B_{ij}, D_{ij}\right) = \sum_{k=1}^{N} \int_{h_{k-1}}^{h_k} (\bar{C}_{ij})_k (1, Z, Z^2) dZ, \tag{12}$$

where $\bar{C}_{ij}$ are coefficients of the transformed stiffness matrix $\bar{\mathbf{C}}$ for the kth layer. They can be calculated from the stiffness coefficients and the ply angle θ,

$$\begin{aligned}
\bar{C}_{11} &= C_{11}\cos^4\theta + (2C_{12} + 4C_{66})\cos^2\theta\sin^2\theta \\
&\quad + C_{22}\sin^4\theta, \\
\bar{C}_{22} &= C_{22}\cos^4\theta + (2C_{12} + 4C_{66})\cos^2\theta\sin^2\theta \\
&\quad + C_{11}\sin^4\theta, \\
\bar{C}_{33} &= C_{33}, \\
\bar{C}_{66} &= (C_{11} + C_{22} - 2C_{12} - 2C_{66})\cos^2\theta\sin^2\theta \\
&\quad + C_{66}(\sin^4\theta + \cos^4\theta), \\
\bar{C}_{12} &= (C_{11} + C_{22} - 4C_{66})\cos^2\theta\sin^2\theta \\
&\quad + C_{12}(\sin^4\theta + \cos^4\theta), \\
\bar{C}_{13} &= C_{13}\cos^2\theta + C_{23}\sin^2\theta, \\
\bar{C}_{16} &= (C_{11} - C_{12} - 2C_{66})\cos^3\theta\sin\theta \\
&\quad + (C_{12} - C_{22} + 2C_{66})\cos\theta\sin^3\theta, \\
\bar{C}_{23} &= C_{23}\cos^2\theta + C_{13}\sin^2\theta, \\
\bar{C}_{26} &= (C_{11} - C_{12} - 2C_{66})\cos\theta\sin^3\theta \\
&\quad + (C_{12} - C_{22} + 2C_{66})\cos^3\theta\sin\theta, \\
\bar{C}_{36} &= (C_{13} - C_{23})\cos\theta\sin\theta,
\end{aligned} \tag{13}$$

The stiffness matrix **C** can be expressed by compliance matrix elements

$$\mathbf{C} = \begin{bmatrix}
\frac{S_{22}S_{33} - S_{23}^2}{S} & \frac{S_{13}S_{23} - S_{12}S_{33}}{S} & \frac{S_{12}S_{23} - S_{13}S_{22}}{S} & 0 \\
\frac{S_{13}S_{23} - S_{12}S_{33}}{S} & \frac{S_{11}S_{33} - S_{13}^2}{S} & \frac{S_{12}S_{13} - S_{23}S_{11}}{S} & 0 \\
\frac{S_{12}S_{23} - S_{13}S_{22}}{S} & \frac{S_{12}S_{13} - S_{23}S_{11}}{S} & \frac{S_{11}S_{22} - S_{12}^2}{S} & 0 \\
0 & 0 & 0 & \frac{1}{S_{66}}
\end{bmatrix}, \tag{14}$$

in which

$$\begin{aligned}
S = {} & S_{11}S_{22}S_{33} - S_{11}S_{23}S_{23} - S_{22}S_{13}S_{13} - S_{33}S_{12}S_{12} \\
& + 2S_{12}S_{13}S_{23},
\end{aligned} \tag{15}$$

where the compliance matrix can be easily obtained from elastic parameters of the composite material

$$\mathbf{S} = \begin{bmatrix}
1/E_{11} & -v_{12}/E_{11} & -v_{13}/E_{11} & 0 \\
-v_{12}/E_{11} & 1/E_{22} & -v_{23}/E_{22} & 0 \\
-v_{13}/E_{11} & -v_{23}/E_{22} & 1/E_{33} & 0 \\
0 & 0 & 0 & 1/G_{12}
\end{bmatrix}. \tag{16}$$

2.3 Dynamic models

As shown in Fig. 2, an auxetic CNTRC laminated beam is in a two-dimensional (2D) plane-coordinate system where X and Z are along the directions of the beam length and thickness, respectively. We assume that $\bar{W}$ and $\bar{\Psi}_x$ are the deflection and the mid-plane rotation of the beam, respectively. Based on the Reddy's higher-order shear deformation theory (Heyliger and Reddy 1988), the dynamic equations of a shear deformable laminated beam considering von-Kármán nonlinearity can be expressed by

$$\begin{aligned}
& s_{11}\frac{\partial^4\bar{W}}{\partial X^4} + s_{12}\frac{\partial^3\bar{\Psi}_x}{\partial X^3} + \frac{\bar{B}_{11}}{\bar{A}_{11}}\frac{\partial^2\bar{N}^T}{\partial X^2} + \frac{\partial^2\bar{M}^T}{\partial X^2} + \bar{N}_x\frac{\partial^2\bar{W}}{\partial X^2} \\
& \quad = Q + I_1\frac{\partial^2\bar{W}}{\partial t^2} + \hat{I}_5\frac{\partial^3\bar{\Psi}_x}{\partial X\partial t^2} - \frac{4}{3h^2}\hat{I}_7\frac{\partial^4\bar{W}}{\partial X^2\partial t^2},
\end{aligned} \tag{17}$$

$$\begin{aligned}
& s_{21}\frac{\partial^3\bar{W}}{\partial X^3} + s_{22}\frac{\partial^2\bar{\Psi}_x}{\partial X^2} - s_{23}\left(\bar{\Psi}_x + \frac{\partial\bar{W}}{\partial X}\right) - s_{26}\frac{\partial\bar{N}^T}{\partial X} + \frac{\partial\bar{S}^T}{\partial X} \\
& \quad = \tilde{I}_3\frac{\partial^2\bar{\Psi}_x}{\partial t^2} - \frac{4}{3h^2}\tilde{I}_5\frac{\partial^3\bar{W}}{\partial X\partial t^2},
\end{aligned} \tag{18}$$

where

$$\bar{N}_x = \frac{1}{L}\int_0^L \left[\frac{\bar{A}_{11}}{2}\left(\frac{\partial \bar{W}}{\partial X}\right)^2 + \bar{B}_{11}\frac{\partial \bar{\Psi}_x}{\partial X} - \frac{4}{3h^2}\bar{E}_{11}\left(\frac{\partial \bar{\Psi}_x}{\partial X} + \frac{\partial^2 \bar{W}}{\partial X^2}\right) - \bar{N}^T\right] dX, \tag{19}$$

and the coefficients s_{11}, s_{12}, et al., are defined by

$$\begin{aligned}
s_{11} &= -\frac{4}{3h^2}\left(\bar{F}_{11} - \frac{\bar{B}_{11}\bar{E}_{11}}{\bar{A}_{11}}\right),\\
s_{12} &= \bar{D}_{11} - \frac{4}{3h^2}\bar{F}_{11} - \frac{\bar{B}_{11}}{\bar{A}_{11}}\left(\bar{B}_{11} - \frac{4}{3h^2}\bar{E}_{11}\right),\\
s_{21} &= -\frac{4}{3h^2}\bar{F}_{11} + \frac{16}{9h^4}\bar{H}_{11} + \frac{4\bar{E}_{11}}{3h^2\bar{A}_{11}}\left(\bar{B}_{11} - \frac{4}{3h^2}\bar{E}_{11}\right),\\
s_{22} &= \bar{D}_{11} - \frac{4}{3h^2}\bar{F}_{11} - \frac{4}{3h^2}\left(\bar{F}_{11} - \frac{4}{3h^2}\bar{H}_{11}\right) - \frac{1}{\bar{A}_{11}}\left(\bar{B}_{11} - \frac{4}{3h^2}\bar{E}_{11}\right)^2,\\
s_{23} &= A_{55} - \frac{4}{h^2}D_{55} - \frac{4}{h^2}\left(D_{55} - \frac{4}{h^2}F_{55}\right),\\
s_{26} &= \frac{\bar{B}_{11}}{\bar{A}_{11}} - \frac{4}{3h^2}\frac{\bar{E}_{11}}{\bar{A}_{11}},
\end{aligned} \tag{20}$$

where $\bar{A}_{11}, \bar{B}_{11}$, and $\bar{D}_{11}$ can be obtained from Eq. (12), while $\bar{E}_{11}$, $\bar{F}_{11}$, and $\bar{H}_{11}$ are respectively defined as

$$(\bar{E}_{11}, \bar{F}_{11}, \bar{H}_{11}) = \sum_{k=1}^{N}\int_{h_{k-1}}^{h_k} (\bar{C}_{11})_k (Z^3, Z^4, Z^6) dZ \tag{21}$$

Here, the definitions of $\bar{A}_{55}$, $\bar{B}_{55}$, and $\bar{D}_{55}$ are

$$(\bar{A}_{55}, \bar{B}_{55}, \bar{D}_{55}) = \sum_{k=1}^{N}\int_{h_{k-1}}^{h_k} (\bar{C}_{55})_k (1, Z, Z^2) dZ \tag{22}$$

where $\bar{C}_{55}$ is equal to G_{13}. In Eqs. (20) and (21), h_k is the z-coordinate of the top surface of the kth ply and h_0 represents the z-coordinate of bottom surface of the beam. In Eqs. (17) and (18), the inertias I_i (i = 1, 2, 3, 4, 5, 7) are defined by

$$(I_1, I_2, I_3, I_4, I_5, I_7) = \sum_{k=1}^{N}\int_{h_{k-1}}^{h_k} \rho_k (1, Z, Z^2, Z^3, Z^4, Z^6) dZ \tag{23}$$

where ρ_k is the mass density of the kth ply, and

$$\begin{aligned}
&\bar{I}_2 = I_2 - \frac{4}{3h^2}I_4, \quad \bar{I}_3 = I_3 - \frac{8}{3h^2}I_5 + \frac{16}{9h^4}I_7, \quad \tilde{I}_3 = \bar{I}_3 - \frac{\bar{I}_2\bar{I}_2}{I_1},\\
&\bar{I}_5 = I_5 - \frac{4}{3h^2}I_7, \quad \tilde{I}_5 = \bar{I}_5 - \frac{\bar{I}_2 I_4}{I_1}, \quad \hat{I}_5 = \tilde{I}_5 - \frac{\bar{I}_2 I_4}{I_1},\\
&\hat{I}_5 = \tilde{I}_3 - \frac{4}{3h^2}\tilde{I}_5, \quad \tilde{I}_7 = I_7 - \frac{I_4 I_4}{I_1}, \quad \hat{I}_7 = \tilde{I}_5 - \frac{4}{3h^2}\tilde{I}_7.
\end{aligned} \tag{24}$$

In Eqs. (17)–(19), $\bar{N}^T$, $\bar{M}^T$, and $\bar{S}^T$ are force, moment, and higher order moment caused by the temperature rise, and defined by

$$(\bar{N}^T, \bar{M}^T, \bar{P}^T) = \sum_{k=1}^{N}\int_{h_{k-1}}^{h_k} (A_x)_k (1, Z, Z^3)\Delta T dZ, \tag{25}$$

$$\bar{S}^T = \bar{M}^T - \frac{4}{3h^2}\bar{P}^T, \tag{26}$$

in which ΔT is the temperature rise from the reference temperature T_0 to the current temperature T and

$$\begin{aligned}
A_x = {} & \bar{C}_{11}(\cos^2\theta\alpha_{11} + \sin^2\theta\alpha_{22}) + \bar{C}_{12}(\sin^2\theta\alpha_{11} + \cos^2\theta\alpha_{22})\\
& + 2\cos\theta\sin\theta\bar{C}_{16}(\alpha_{11} - \alpha_{22}),
\end{aligned} \tag{27}$$

where α_{11} and α_{22} are in-plane thermal expansion coefficients.

The longitudinal vibration of the impactor can be neglected in the analysis of LVI. Hence, the motion equation of the impactor can be described by Newton's Law as

$$m^i\ddot{W}^i(t) + F_c(t) = 0, \tag{28}$$

and the corresponding initial conditions for its displacement and velocity are set to zero.

2.4 CNTRC material models

A single CNTRC layer where CNTs are aligned can be treated as an orthotropic material. The in-plane material properties of this CNTRC layer, such as elastic and shear moduli can be estimated based on an extended mixture law (Shen 2009). The detailed expressions are written as

$$
\begin{aligned}
E_{11} &= \eta_1 V_{cnt} E_{11}^{cnt} + V_m E^m,\\
\frac{\eta_2}{E_{22}} &= \frac{V_{cnt}}{E_{22}^{cnt}} + \frac{V_m}{E^m},\\
\frac{\eta_3}{G_{12}} &= \frac{V_{cnt}}{G_{12}^{cnt}} + \frac{V_m}{G^m},
\end{aligned}
\tag{29}
$$

and the in-plane Poisson's ratio v_{12} is written as

$$
v_{12} = V_{cnt} v_{12}^{cnt} + V_m v^m, \tag{30}
$$

where E_{11}, E_{22}, and G_{12} are elastic moduli and shear modulus, respectively, of a CNTRC layer. The superscript or subscript *cnt* denotes carbon nanotube, while *m* denotes matrix. V is the volume fraction of component (reinforcement or matrix) in the composite and $V_{cnt} + V_m = 1$. It is worth noting that efficiency parameters η_i ($i = 1$, 2 and 3) are introduced in Eq. (29) to take into account the small-scale effect.

3 Solution method

A two-step perturbation technique is adopted herein to solve the governing equations obtained in Sect. 2. For convenience, the following dimensionless parameters are introduced

$$
\begin{aligned}
&x = \pi\frac{X}{L}, W = \frac{\bar{W}}{L}, \Psi_x = \frac{\bar{\Psi}_x}{\pi}, N_x = \frac{L^2\bar{N}_x}{\pi^2\bar{D}_{11}},\\
&(M_x, P_x) = \frac{L^2}{\pi^2 h\bar{D}_{11}}\left(\bar{M}_x, \frac{4}{3h^2}\bar{P}_x\right),\\
&(\gamma_{11}, \gamma_{12}, \gamma_{21}, \gamma_{22}) = \frac{1}{\bar{D}_{11}}(-s_{11}, s_{12}, -s_{21}, s_{22}),\\
&\omega_L = \Omega_L\frac{L}{\pi}\sqrt{\frac{\rho_0}{E_0}},\\
&\gamma_{23} = \frac{L^2}{\pi^2\bar{D}_{11}}s_{23}, \gamma_{13} = \frac{L^2\bar{A}_{11}}{\pi^2\bar{D}_{11}}, (\gamma_{14}, \gamma_{15})\\
&\quad = \frac{L}{\pi^2\bar{D}_{11}}\left(\bar{B}_{11} - \frac{4}{3h^2}\bar{E}_{11}, \frac{4}{3h^2}\bar{E}_{11}\right),\\
&(\gamma_{16}, \gamma_{26}) = \frac{1}{\bar{A}_{11}L}\left(\bar{B}_{11}, \bar{B}_{11} - \frac{4}{3h^2}\bar{E}_{11}\right),\\
&\gamma_{17} = -\frac{I_1 E_0 L^2}{\pi^2\rho_0\bar{D}_{11}}, V_0 = \frac{\bar{V}_0}{\pi}\sqrt{\frac{\rho_0}{E_0}},\\
&(\gamma_{18}, \gamma_{19}, \gamma_{28}, \gamma_{29}) = -(\tilde{I}_5, -\frac{4}{3h^2}\tilde{I}_7, \tilde{I}_3, -\frac{4}{3h^2}\tilde{I}_5)\frac{E_0}{\rho_0\bar{D}_{11}}, t = \frac{\pi\bar{t}}{L}\sqrt{\frac{E_0}{\rho_0}},\\
&\gamma_{T1}\Delta T = \frac{L^2 A_x^T\Delta T}{\pi^2\bar{D}_{11}}, (\gamma_{T3}, \gamma_{T6})\Delta T\\
&\quad = \frac{L^2\Delta T}{\pi^2 h\bar{D}_{11}}\left(D_x^T, \frac{4}{3h^2}F_x^T\right), \lambda_q = \frac{F_c bL}{\pi^2\bar{D}_{11}},
\end{aligned}
\tag{31}
$$

in which $\bar{W}^*$ is the initial deflection which is caused by the temperature variation and the geometrically imperfection in the present case. ρ_0 and E_0 are herein the reference values of ρ^m and E^m at the room temperature (T = 300 K).

To simplify the perturbation procedure, $\tau = \varepsilon t$ is introduced after dimensionless process. By employing Eqs. (31), (17) and (18) may then be rewritten in the following dimensionless form

$$
\begin{aligned}
&\gamma_{11}\frac{\partial^4 W}{\partial x^4} - \gamma_{12}\frac{\partial^3\Psi_x}{\partial x^3}\\
&- \pi\left\{\int_0^\pi\left[\frac{\gamma_{13}}{2}\left(\frac{\partial W}{\partial x}\right)^2 + \gamma_{14}\frac{\partial\Psi_x}{\partial x} - \gamma_{15}\frac{\partial^2 W}{\partial x^2}\right]dx\right\}\frac{\partial^2 W}{\partial x^2}\\
&\quad + \gamma_{T1}\Delta T\frac{\partial^2 W}{\partial x^2} - \gamma_{16}\frac{\partial^2 N^T}{\partial x^2} - \gamma_{T3}\Delta T\frac{\partial^2 M^T}{\partial x^2}\\
&\quad = \lambda_q + \gamma_{17}\frac{\partial^2 W}{\partial\tau^2} + \gamma_{18}\frac{\partial^3\Psi_x}{\partial x\partial\tau^2} + \gamma_{19}\frac{\partial^4 W}{\partial x^2\partial\tau^2},
\end{aligned}
\tag{32}
$$

$$
\begin{aligned}
&\gamma_{21}\frac{\partial^3 W}{\partial x^3} - \gamma_{22}\frac{\partial^2\Psi_x}{\partial x^2} + \gamma_{23}\left(\Psi_x + \frac{\partial W}{\partial x}\right) - \gamma_{26}\frac{\partial N^T}{\partial x}\\
&\quad - (\gamma_{T3} - \gamma_{T6})\Delta T\frac{\partial^2 M^T}{\partial x^2}\\
&\quad = \gamma_{28}\frac{\partial^2\Psi_x}{\partial\tau^2} + \gamma_{29}\frac{\partial^3 W}{\partial x\partial\tau^2}.
\end{aligned}
\tag{33}
$$

Since two ends of the beam are simply supported, the boundary conditions are written as

$$
W|_{\tau=0} = \left.\frac{\partial W}{\partial\tau}\right|_{\tau=0} = 0, \quad M_x|_{\tau=0} = \left.\frac{\partial M_x}{\partial\tau}\right|_{\tau=0} = 0. \tag{34}
$$

The solutions of the deflection and the rotation can be both divided into two parts as

$$
W(x,\tau) = W^*(x) + \tilde{W}'(x,\tau), \tag{35}
$$

$$
\Psi_x(x,\tau) = \Psi_x^*(x) + \tilde{\Psi}_x'(x,\tau), \tag{36}
$$

in which $\tilde{W}'(x,\tau)$ is an additional deflection caused by LVI while $W^*(x)$ is an initial deflection due to initial thermal bending moment. $\tilde{\Psi}_x'(x,\tau)$ and $\Psi_x^*(x)$ are the mid-plane rotations corresponding to $\tilde{W}'(x,\tau)$ and $W^*(x)$, respectively. Note that $W^*(x)$ and $\Psi_x^*(x)$ are equal to 0 at room temperature and can be obtained through solving thermal bending equations reported in

Fan and Wang (2016). In such a case, Eqs. (32) and (33) can be rewritten as

$$\begin{aligned}
&\gamma_{11}\frac{\partial^4 W'}{\partial x^4}-\gamma_{12}\frac{\partial^3 \tilde{\Psi}'_x}{\partial x^3}\\
&-\pi\left\{\int_0^{\pi}\left[\frac{\gamma_{13}}{2}\left(\frac{\partial \tilde{W}'}{\partial x}\right)^2+\gamma_{14}\frac{\partial \tilde{\Psi}'_x}{\partial x}-\gamma_{15}\frac{\partial^2 \tilde{W}'}{\partial x^2}\right]dx\right\}\\
&\left(\frac{\partial^2 \tilde{W}'}{\partial x^2}+\frac{\partial^2 W^*}{\partial x^2}\right)\\
&\quad-\pi\left\{\int_0^{\pi}\left[\frac{\gamma_{13}}{2}\left(2\frac{\partial W'}{\partial x}\frac{\partial W^*}{\partial x}+\left(\frac{\partial W^*}{\partial x}\right)^2\right)+\gamma_{14}\frac{\partial \Psi^*_x}{\partial x}-\gamma_{15}\frac{\partial^2 W^*}{\partial x^2}\right]dx\right\}\frac{\partial^2 W'}{\partial x^2}\\
&=\lambda_q+\varepsilon^2\left(\gamma_{17}\frac{\partial^2 W'}{\partial \tau^2}+\gamma_{18}\frac{\partial^3 \tilde{\Psi}'_x}{\partial x\partial \tau^2}+\gamma_{19}\frac{\partial^4 W'}{\partial x^2\partial \tau^2}\right),
\end{aligned}\tag{37}$$

$$\begin{aligned}
&\gamma_{21}\frac{\partial^3 W'}{\partial x^3}-\gamma_{22}\frac{\partial^2 \Psi'_x}{\partial x^2}+\gamma_{23}\left(\Psi'_x+\frac{\partial W'}{\partial x}\right)\\
&=\varepsilon^2\left(\gamma_{28}\frac{\partial^2 \Psi'_x}{\partial \tau^2}+\gamma_{29}\frac{\partial^3 W'}{\partial X\partial \tau^2}\right).
\end{aligned}\tag{38}$$

Using a two-step perturbation technique, the solutions can be written in the following forms

$$\begin{aligned}
W'(x,\tau,\varepsilon)&=\sum_{j=1}\varepsilon^j w_j(x,\tau),\\
\Psi'_x(x,\tau,\varepsilon)&=\sum_{j=1}\varepsilon^j \psi_{xj}(x,\tau),\\
\lambda_q(x,\tau,\varepsilon)&=\sum_{j=1}\varepsilon^j \lambda_j(x,\tau).
\end{aligned}\tag{39}$$

where ε is a small perturbation parameter without any physical meaning. Using Eq. (39), a set of perturbation equations for the different order of ε can be obtained and solved order by order. We obtain the asymptotic solutions

$$W'=\varepsilon A_{10}^{(1)}\sin mx+O(\varepsilon^4),\tag{40}$$

$$\begin{aligned}
\Psi'_x=&\varepsilon B_{10}^{(1)}\cos mx+\varepsilon^2 B_{10}^{(2)}\cos mx+\varepsilon^3 B_{10}^{(3)}\cos mx\\
&+O(\varepsilon^4),
\end{aligned}\tag{41}$$

$$\begin{aligned}
\lambda_q=&[g_{30}\varepsilon\ddot{A}_{10}^{(1)}+g_{31}\varepsilon A_{10}^{(1)}]\sin mx\\
&+[\left(\varepsilon A_{10}^{(1)}\right)^3 g_{331}+\left(\varepsilon A_{10}^{(1)}\right)^2\varepsilon A_{10}^{*}g_{332}]\sin mx+O(\varepsilon^4).
\end{aligned}\tag{42}$$

We take $x=\pi/2$, which is the impact location. The second perturbation parameter $\left(\varepsilon A_{10}^{(1)}\right)$ in Eq. (42) can be replaced by the maximum dimensionless deflection of the beam W_m through Eq. (40). After applying the Galerkin method, Eq. (42) can be rewritten as

$$\begin{aligned}
&g_{30}\frac{d^2(W_m)}{d\tau^2}+g_{31}(W_m)+g_{32}(W_m)^2+g_{33}(W_m)^3\\
&=g_q(W^i-W_m)^{\frac{3}{2}}.
\end{aligned}\tag{43}$$

After the process of non-dimensioning, Eq. (28) can be rewritten as

$$\ddot{W}^i=g_i(W^i-W_m)^{3/2}.\tag{44}$$

A fourth order Runge–Kutta numerical method is used to solve Eqs. (43) and (44). All symbols used in Eqs. (43) and (44) is described in detail in "Appendix B".

4 Parametric studies and discussion

In this section, the numerical examples of the LVI for the CNTRC laminated beams with various parameters are presented. The beam with $b=1$ mm and $L=15$ mm is simply supported on both ends. As is mentioned before, CNTRC is assumed to be temperature-dependent and the material properties for the matrix are $\nu^m=0.34$, $\alpha^m=45(1+0.0005\Delta T)\times 10^{-6}$ K^{-1}, $E^m=(3.51-0.0047T)$ GPa, and $\rho^m=1150$ kg/m^3. The single-walled carbon nanotubes are chosen as the reinforcements and their temperature-dependent material properties are listed in Table 1 (Han and Elliott 2007). In our computation, three volume fractions ($V_{cnt}=0.11$, 0.14, and 0.17) of CNTs are considered and the corresponding efficiency parameters are given as (Shen 2009)

$$\begin{aligned}
V_{cnt}=0.11:&\ \eta_1=0.149,\quad \eta_2=0.934,\quad \eta_3=0.934,\\
V_{cnt}=0.14:&\ \eta_1=0.150,\quad \eta_2=0.941,\quad \eta_3=0.941,\\
V_{cnt}=0.17:&\ \eta_1=0.149,\quad \eta_2=1.381,\quad \eta_3=1.381.
\end{aligned}$$

In addition, we assume that a single CNTRC ply satisfy the transversely isotropy with $\nu_{23}=0.48$ in the out-of-plane direction.

To investigate the effect of FG of the CNT, we modeled the FG-CNTRC using a piece-wise method to create the functionally grading profile of the CNT across the thickness. Two FG patterns, namely, FG-X and FG-O, are created and their NPR effects and the LVI responses are studied and compared. Note that this piece-wise method has also been used in the previous work (Fan et al. 2018a, b) for modeling

Table 1 Temperature-dependent material properties for single-walled CNT (Han and Elliott 2007) ($v_{12}^{\mathrm{CN}} = 0.175$, $\rho^{CN} = 1750$ kg/m^3)

T (K)	E_{11}^{CN} (TPa)	E_{22}^{CN} (TPa)	G_{12}^{CN} (TPa)	α_{11}^{CN} ($\times 10^{-6}$/K)	α_{22}^{CN} ($\times 10^{-6}$/K)
300	5.6466	7.0800	1.9445	3.4584	5.1682
400	5.5679	6.9814	1.9703	4.1496	5.0905
500	5.5308	6.9348	1.9643	4.5361	5.0189

functionally graded graphene reinforced composite structures. For FG-X, the volume fraction of CNT for each layer along the thickness direction is [0.17/0.14/0.11/0.14/0.17]; for FG-O, the volume fractions of all five layers are [0.11/0.14/0.17/0.14/0.11]. When the volume fractions of CNT are the same for all the layers in a beam, it is referred to as UD (i.e., uniform distribution). Unless otherwise stated, the material properties for the CNTRC laminated beam and assumptions mentioned above are used in the following examples.

4.1 Validation of the developed theoretical model against FEA

Before carrying out parametric studies, we have to test the effectiveness and accuracy of the present method. The layup of the beam is $[\theta/-\theta/\theta/-\theta/\theta]$ and θ is ply angle that can be changed from 0 to 90. Utilizing the commercial software ABAQUS, a finite element analysis (FEA) is carried out to calculate the effective out-of-plane Poisson's ratio v_{13}^{e} with various ply angle θ. In our finite element model, a three-dimensional solid computational domain of 15 mm long, 1 mm wide, and 5 mm thick was created and partitioned into 5 individual layers. The thickness of each layer is 0.1 mm. The stacking sequence of the laminate was defined by the orientation of each layer at the integration point. Since 5 layers were obtained by partitioning a complete solid domain, the adjacent layers share the same nodes at the interface boundary which conforms to the perfect bonding assumption. Figure 3 shows good agreement of v_{13}^{e} between the results obtained from the present method and FEA. Besides, it can be found that the NPR of the laminate is generated in the range of ply angle from 7 to 44 and the minimal value of NPR reaches lower than -1 at a ply angle of around 20. The CNTRC laminate with an asymmetric layup $[\theta/-\theta]_3$ is also studied. The results

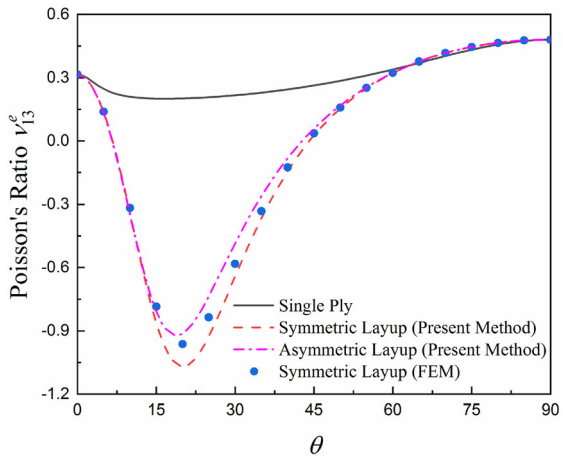

Fig. 3 The effective Poisson's ratio, v_{13}^{e}, of $[\theta/-\theta/\theta/-\theta/\theta]$ and $[\theta/-\theta]_3$ CNTRC laminate beams

depicted in Fig. 3 show that the asymmetric layup $[\theta/-\theta]_3$ can also produce the effective out-of-plane NPR. In addition to the asymmetric CNTRC laminate, we have also performed NPR studies on the quasi-isotropic and cross-ply layup CNTRC laminates. However, results showed that the NPRs do not exist for those layups. It appears that only layups consisting of alternating θ and $-\theta$ layers are prone to produce NPRs for the considered CNTRC laminates.

Our aforementioned analysis shows that the CNTRC laminate produces most significant NPR effect when the ply angle is close to 15. Therefore, the stacking sequence of [15/− 15/15/− 15/15] is herein selected for the beam to study the NPR effect on the LVI response. Similarly, we first present the comparison of LVI between theoretical results and finite element results (as shown in Fig. 4) as another validation. In the FEA, the impactor was modeled as a rigid shell with a semi-spherical shape and discretized using the 4-node 3-D bilinear rigid quadrilateral elements (i.e., R3D4 element in ABAQUS). The CNTRC laminate beam was discretized using the

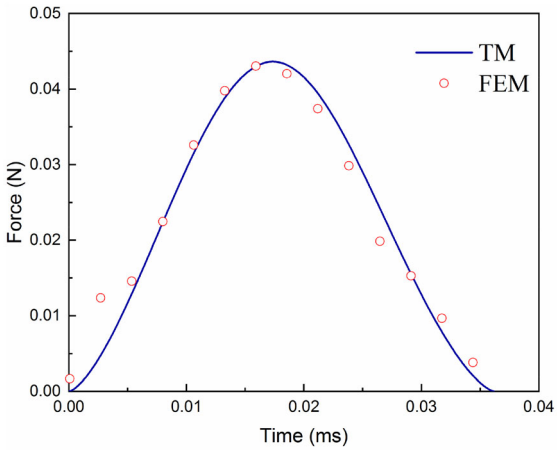

Fig. 4 The results of dimensionless historical force within contact obtained by theoretical method (TM) and FEA

8-node linear brick, reduced integration, hourglass control elements (i.e., C3D8R elements in ABAQUS). The meshing results in a total of 63,906 elements. The contact between the impactor and the CNTRC laminate beam was enforced using the General Contact algorithm of Abaqus/Explicit, which defines a linear pressure-overclosure relationship between the contacting surfaces. The friction coefficient for contacts between the metal impactor and a composite material is taken as 0.3. The same approach of defining the contact in ABAQUS was used in (Pham et al. 2020; González et al. 2012). The impact problem was solved using the Dynamic, Explicit step in ABAQUS. The impactor has an initial velocity of 0.1 m/s and a mass of 0.01 g for the theoretical model and the FEA. It should be noted that in this case, Eq. (5) for calculating contact modulus should be modified as

$$\frac{1}{E^*} = \frac{1}{E_i^b}. \tag{45}$$

Note that the geometry and material properties of CNTRC layer are the same as those used in the previous section. From Fig. 4, good agreement between the results from theoretical method and FEA is found.

To compare the impact responses between the auxetic beam (i.e., beam with NPR) and the nonauxetic beam (i.e., beam with positive Poisson's ratio (PPR), we performed additional study cases for the composite beams with the stacking sequences of [45/− 45/45/− 45/45] and [75/− 75/75/− 75/75]. These two stacking sequences enable the composite beam to produce positive out-of-plane Poisson's ratios, $\nu_{13}^e = 0.0265$ ([45/− 45/45/− 45/45]) and $\nu_{13}^e = 0.44567$ ([75/− 75/75/− 75/75]) (as shown in Fig. 3). A comparison of the obtained deflections for the three cases subjected to LVI is illustrated in Fig. 5. The reduced deflection of the auxetic beam is also visualized using FEA as depicted in the inset of Fig. 5. Note that the deflection is a scaled-up illustration of the deformation and does not represent the true deformation of the beam. The true deformation is only about a few micrometers (see Fig. 5) and cannot be visually observed. The scaled-up deformation allowed us to better visually observe the effect of the NPR on the beam deformation. Figure 6 shows the stress distributions of the [15/− 15/15/− 15/15] auxetic beam and [75/− 75/75/− 75/75] nonauxetic beam at different times subjected to LVI. Note that the impactor was not displayed during the impact for a better illustration of the stress distribution in the CNTRC laminate beams.

This reduced elastic deflection is due to the mechanism of NPR effect, i.e., the material flows into the vicinity of the impact location (see Fig. 2). It can also be explained by checking Eqs. (8) and (9) where a negative Poisson's ratio yields a larger E_i^b, and thus a larger E^* [see Eq. (5)], which results in a larger contact stiffness K_c [see Eq. (4)] and hence a higher contact force F_c [see Eq. (1)]. On the contrary, the material below impact location flows away in the

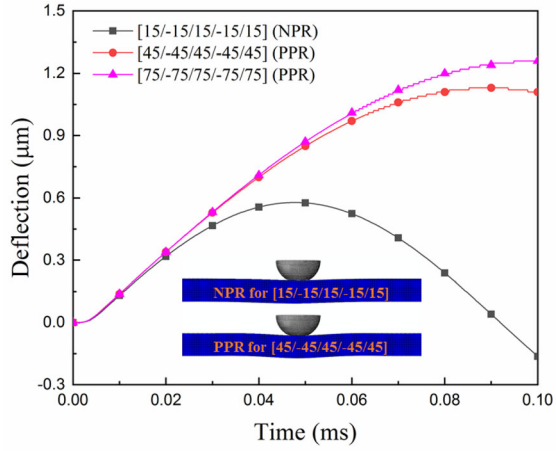

Fig. 5 The historical deflections of the [15/−15/15/−15/15] auxetic beam (with NPR), the [45/−45/45/−45/45] and the [75/−75/75/−75/75] nonauxetic beam (with PPR)

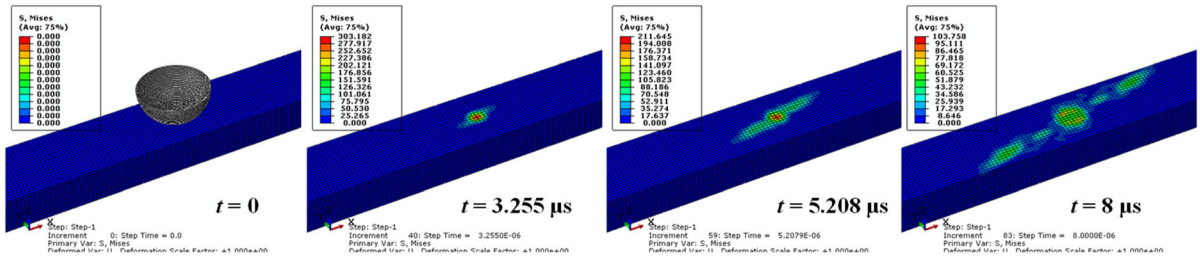

(a) [15/-15/15/-15/15] auxetic CNTRC laminate beam (NPR)

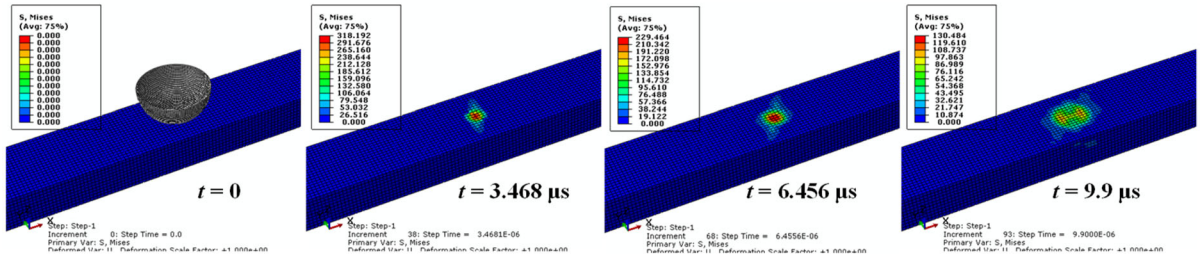

(b) [75/-75/75/-75/75] nonauxetic CNTRC laminate beam (PPR)

Fig. 6 Stress distributions of the [15/−15/15/−15/15] auxetic laminate beam and [75/−75/75/−75/75] nonauxetic laminate beam at different times subjected to LVI (unit in MPa) (the impactor was not displayed during the impact)

lateral direction in the nonauxetic beam. In summary, both theoretical results and finite element results indicate that NPR (i.e., auxeticity) can reduce the indentation, thereby potentially improving the impact resistance of the CNTRC laminated beam.

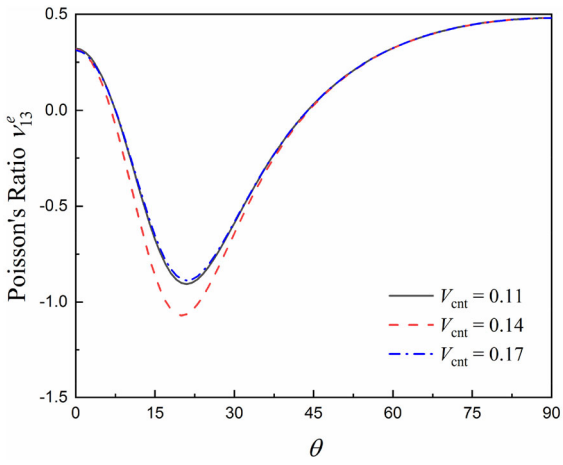

Fig. 7 The effect of CNT volume fraction on effective Poisson's ratio v_{13}^e of a [θ/−θ/θ/−θ/θ] CNTRC laminated beam

4.2 The effect of CNT volume fraction on NPR and LVI response

The effect of CNT volume fraction on Poisson's ratio v_{13}^e is shown in Fig. 7. In the figure, we compare the out-of-plane Poisson's ratio with three different volume fractions of CNT for each layer and it can be seen that the NPR obtained with 0.11 CNT volume fraction is very close to that with 0.17 CNT volume fraction. This shows that increasing the CNT volume fraction does not necessarily enhance the NPR effect. An interesting finding is that the NPR is lower than − 1, only when the V_{cnt} for each layer is equal to 0.14. This phenomenon caused by small-scale effect (Han and Elliott 2007) is not unique and it can be also found in Shen's work (Shen 2009), where the CNTRC beam with 0.14 CNT volume fraction shows the lowest deflection in bending behavior. According to the small-scale effect, the material properties of the composite do not linearly increase if the volume fraction of CNT linearly increases. The effective out-of-plane Poisson's ratios can be determined using Eqs. (10a) and (10b), which are expressed as functions of J_{11}, J_{22}, J_{32}, and J_{31} (i.e., elements in the **J** matrix). The **J** matrix can be determined using the classical **A**, **B**, and **D** laminate stiffness matrices from Eq. (11).

The volume fraction of the CNT affects the engineering constants of each lamina (e.g., E_{11}, E_{22}, and G_{12}), leading to changes in **A**, **B**, **D** matrices of the composite laminate, and hence, changes in the effective out-of-plane Poisson's ratios. However, the **A**, **B**, **D** matrices of the composite laminate reflects a complicated combined effects of the engineering constants and stacking sequence, and thus, making it difficult to identify a simple straightforward relation between the CNT volume fraction and out-of-plane Poisson's ratios. In following examples, only 0.14 volume fraction of CNT is selected for each layer if there is no otherwise statement (Table 2).

Note that the rigid body impactor was only used in the aforementioned FEA and theoretical analysis aiming to verify the accuracy of our analytical derivations in the developed theoretical model. This is because the assumption of the rigid body enables a more convenient numerical convergence during the FEA implementation and avoids potential numerical issues raised by contact penetrations. In the following examples, the impactor is no longer a rigid body and assumed to be made of steel in the subsequent theoretical analysis of LVI. The material properties of the steel impact is: E^i = 207 GPa, v^i = 0.3, and ρ^i = 7960 kg/m^3. The contact modulus between the steel impactor and the CNTRC laminate beam is described using Eq. (5). The geometry of the impactor is spherical with the radius equaling the width of the beam. Unless otherwise stated, the initial velocity of the impactor is taken to be 5 m/s. Figure 8 shows the influences of CNT volume fraction on both the contact force and indentation. Three volume fractions of CNT for each layer, i.e., 0.11, 0.14, and 0.17, are considered in this case study. It is found that the beam with a V_{cnt} = 0.17 in each layer exhibits the highest peak contact force and the lowest indentation. In particular, the peak contact force increased by 19% and the indentation decreased by 16% when the volume fraction changes from 0.11 to 0.17. It is interesting to note that the beam with 0.14 CNT volume fraction which shows the most significant auxeticity (as shown in Fig. 7) does not produce the best LVI behavior. This is because the stiffness of the beam is also changed when different CNT volume fractions are used and this stiffness effect seems to dominate in this case. To further address the conflict of the 0.14 CNT volume fraction case gives the best NPR but not the best LVI behavior, it is essential to understand the different effects of NPR and stiffness on the LVI behavior of the CNTRC laminates. However, the dilemma is that if one changes the CNT volume fraction, it simultaneously changes the stiffness and the value of the NPR of the CNTRC laminate. Therefore, it is quite

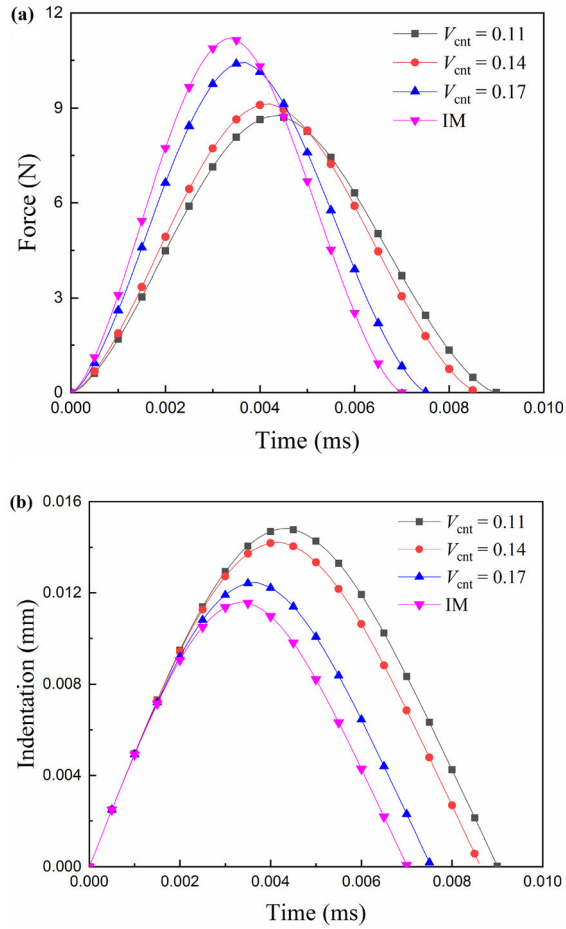

Fig. 8 The effect of CNT volume fraction of the [15/−15/15/−15/15] auxetic nanocomposite beam: **a** historical contact force; **b** historical indentation

Table 2 The values of J_{11} and J_{31}, and out-of-plane Poisson's ratios of [15/−15/15/−15/15] CNTRC laminated beams with CNT volume fractions ranging from 0.11 to 0.17

	V_{cnt} = 0.11	V_{cnt} = 0.14	V_{cnt} = 0.17
J_{11} (m/N)	15.398	12.511	9.978
J_{31} (m/N)	10.377	10.798	6.524
v^e_{13}	− 0.673	− 0.863	− 0.654

challenging to study the individual effect of NPR and stiffness on the LVI behavior of the auxetic CNTRC laminate separately. To address this, we created an imaginary CNTRC laminate beam (IM beam) having an NPR same with the one produced by the 0.14 CNT volume fraction laminate but having the moduli same with the 0.17 CNT volume fraction laminate. Therefore, if one compares the results between the IM laminate and the 0.14 CNT volume fraction laminate, the effect of the moduli can be observed. Meanwhile, if one compares the results between IM laminate and the 0.17 CNT volume fraction laminate, the effect of the NPR can be observed. This additional IM beam case is analyzed using the same developed theoretical model. The new results for this IM beam are obtained and compared with the results for the CNTRC laminate beams with 0.14 and 0.17 CNT volume fractions. The comparison is shown in Fig. 8. As one can see, both higher moduli and the NPR can improve the LVI behavior by comparing the historical force and indentation curves, respectively. It also can be noticed that the increased stiffness from 0.14 CNT volume fraction to 0.17 CNT volume fraction has a more significant contribution to the LVI behavior compared with the increased NPR. Therefore, this explains the conflict that the 0.14 CNT volume fraction case shows the lowest NPR but not the best LVI behavior. However, it is worth noting that the above discussion is only true and meaningful within the present material system.

4.3 The effect of FG pattern on NPR and LVI response

Figure 9 depicts the out-of-plane Poisson's ratio affected by different FG patterns. Regardless of FG-X or FG-O distributions, the NPR effect is not as pronounced as that for the UD composite. Results of the FG pattern effect on LVI responses of the CNTRC beam is illustrated in Fig. 10. Since changing the FG pattern also changes the stiffness of the composite, this example also demonstrates the coupling effect between the stiffness and the NPR, which, as mentioned in the previous example, is the potential cause for the 0.14 CNT volume fraction being the best one for auxeticity but not the one for highest peak force and lowest indentation. Here, it is also interesting to note that our results indicate the FG-O beam possesses the best dynamic response under the LVI loading.

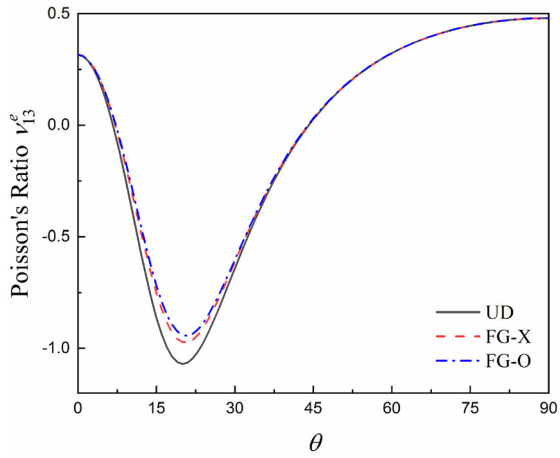

Fig. 9 The effect of FG pattern on effective Poisson's ratio v_{13}^e of a $[\theta/-\theta/\theta/-\theta/\theta]$ auxetic CNTRC laminated beam

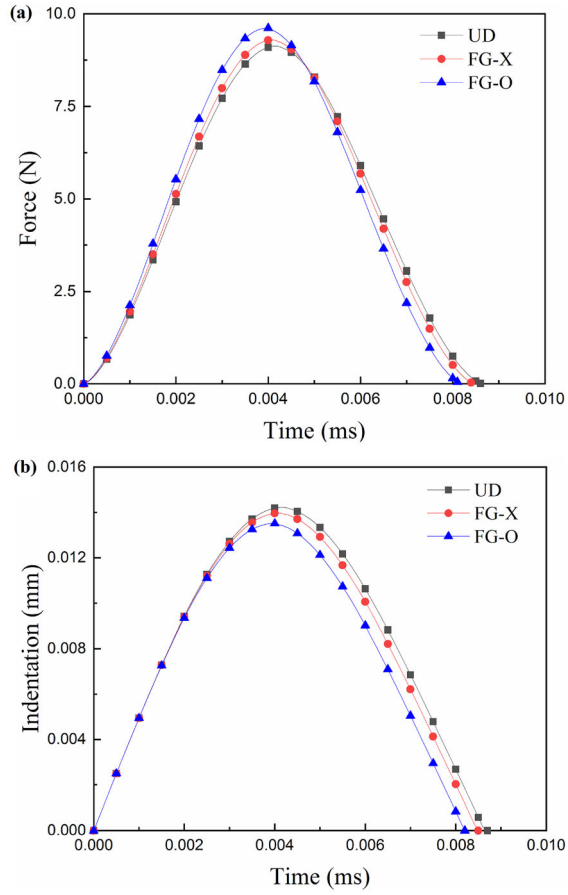

Fig. 10 The effect of FG pattern of the [15/−15/15/−15/15] auxetic nanocomposite beam: **a** historical contact force; **b** historical indentation

Such a finding is different from those reported in the previous work (Fan and Wang 2016; 2017b) in which they reported that the FG-X beam shows the best dynamic response. This inconsistency could also be due to the coupling effects between the stiffness and the NPR effect, which will be further discussed and verified in our next research project.

4.4 The thermal effect on NPR and LVI response

Figure 11 illustrates the temperature influence on the NPR of a UD beam with V_{cnt} = 0.14. We find that the NPR effect will be more significant when the temperature is increased. In particular, the Poisson's ratio decreased by 51.5% when temperature increases from 300 to 500 K. It can be noticed that the NPR even exceeds − 1.5 at 500 K. Finally, the dynamic behaviors of the FG-O CNTRC beam under different temperature is illustrated in Fig. 12. The results show that the peak impact force of the beam reduced by 14.8% and the indentation increased by 17.5% when the temperature is increased from 300 K to 500 K. To estimate the effectiveness of the thermoelastic stiffening, the deflection vs. load at different temperatures is plotted in Fig. 12c. It can be seen that the stiffening increases as the temperature decreases. However, this stiffening effect is not linear. More significant loss of stiffening is observed when temperature decreases from 400 to 300 K than the loss when temperature decreases from 500 to 400 K. This nonlinear behavior is closely related to the nonlinear temperature-dependent thermal expansion coefficient of the CNTRC laminate (see Table 1).

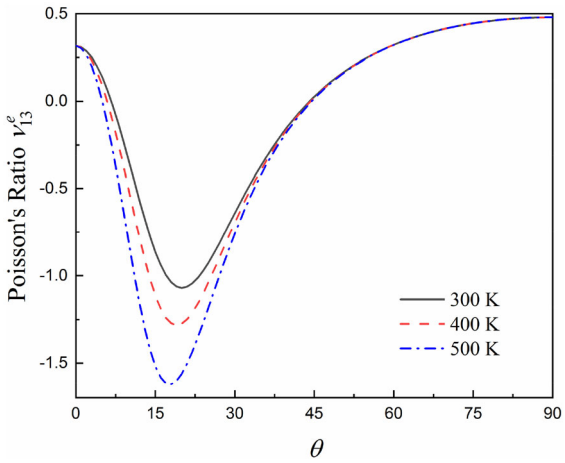

Fig. 11 The effect of temperature on effective Poisson's ratio ν_{13}^e of a $[\theta/-\theta/\theta/-\theta/\theta]$ auxetic CNTRC laminated beam

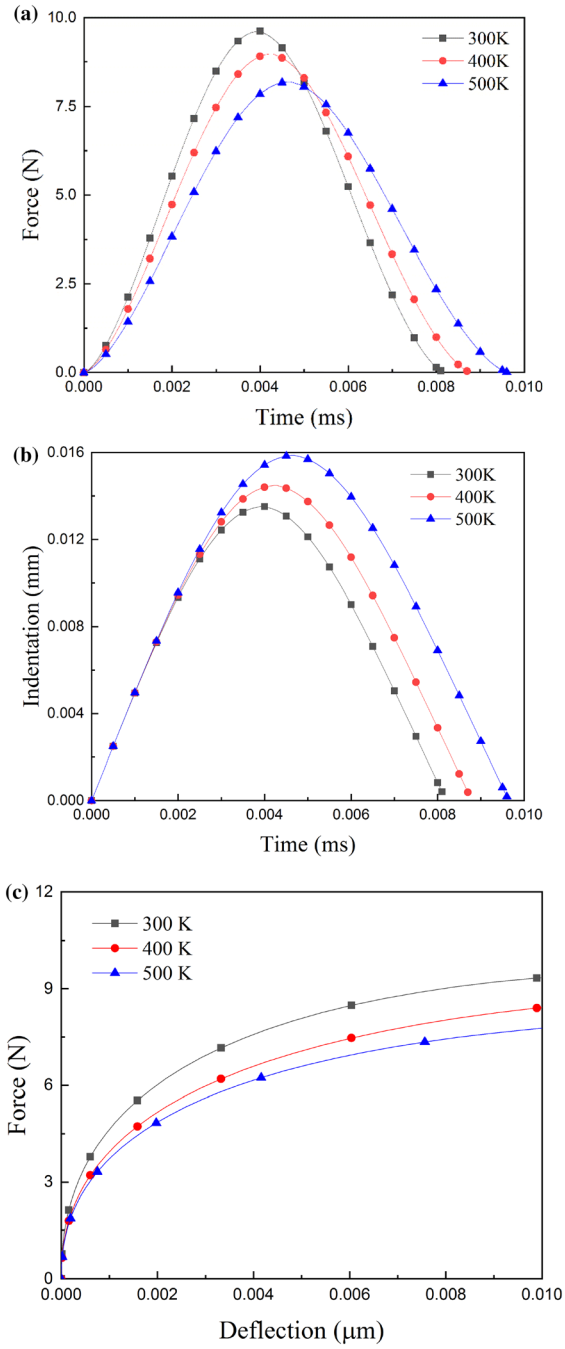

Fig. 12 The effect of temperature of the [15/−15/15/−15/15] auxetic nanocomposite beam: **a** historical contact force; **b** historical indentation; **c** force versus deflection

In summary, from Figs. 7, 9, and 11, it is evident that the out-of-plane Poisson's ratio can be greatly

affected by the CNT volume fraction, temperature, and the FG pattern. Similarly, we find that the effects of CNT volume fraction, FG pattern, and temperature on LVI response of the auxetic nanocomposite beam are also quite significant from the relevant parametric studies (see Figs. 8, 10, and 12).

5 Conclusions

The LVI response of an auxetic CNTRC laminated beam with the out-of-plane NPR is investigated in this paper. The contact process is modeled by a newly developed Hertzian law to take into account the out-of-plane Poisson's ratio effect. The theoretical models for NPR and LVI are both established. In addition to the theoretical analysis, FEA is also employed to verify the theoretical results and visually observe the NPR effect. Both theoretical and finite element results indicate that the auxetic beam leads to reduced elastic deformation and increased impact force than nonauxetic beams. Moreover, our results show that the NPR effect and the dynamic performance of the NPR beam are sensitive to the CNT volume fraction, beam FG pattern, and temperature. From our parametric study, the laminated beam with a volume fraction of 0.14 shows the largest auxetic property among the three CNT volume fractions we considered (i.e., 0.11, 0.14, and 0.17) and this property would be further enhanced by increasing the temperature. However, this beam does not show the best behavior under the LVI due to the concurrent change of the stiffness. Furthermore, the temperature rise causing material softening could potentially reduce the indentation resistance. Lastly, our results show that the effect of FG distribution on the NPR is limited and the FG-O beam exhibits a comparably better LVI performance when compared to the FG-X and UD beams. It is worth stressing that the reduced elastic deflection and increased impact peak force observed from the auxetic composites do not translate directly to improved impact resistance. Further nonlinear analysis incorporating appropriate failure criteria needs to be performed to investigate the effect of NPR on the impact resistance of the CNTRC laminate beams.

The novel theoretical models developed in this study as well as the results and discussions are expected to facilitate the design of advanced auxetic nanocomposite materials. Such composites are potential ideal material candidates for next generation lightweight automotive and aerospace structures with exceptional indentation and impact resistance capabilities.

Acknowledgements The authors wish to acknowledge the Marvin B. Dow Advanced Composites Institute at Mississippi State University for providing the financial support of this project. Y. Wang thanks many helpful discussions with Dr. Barry Davidson (Professor at Mechanical and Aerospace Engineering Department, Syracuse University).

Data availability Data will be made available upon request.

Appendix A

For the laminate with arbitrary layup, the relation between load and deformation is written as

$$\begin{Bmatrix} \mathbf{N} \\ \mathbf{M} \end{Bmatrix} = \begin{bmatrix} \mathbf{A} & \mathbf{B} \\ \mathbf{B} & \mathbf{D} \end{bmatrix} \begin{Bmatrix} \boldsymbol{\varepsilon} \\ \boldsymbol{\kappa} \end{Bmatrix} \tag{A.1}$$

From Eq. (A.1), we have

$$\boldsymbol{\varepsilon} = \mathbf{A}^{-1}\mathbf{N} - \mathbf{A}^{-1}\mathbf{B}\boldsymbol{\kappa} \tag{A.2}$$

$$\mathbf{M} = \mathbf{B}\boldsymbol{\varepsilon} + \mathbf{D}\boldsymbol{\kappa} = \mathbf{B}\mathbf{A}^{-1}\mathbf{N} + (\mathbf{D} - \mathbf{B}\mathbf{A}^{-1}\mathbf{B})\boldsymbol{\kappa} \tag{A.3}$$

Equations (A.2) and (A.3) can be rewritten in the form of matrix and vectors

$$\begin{Bmatrix} \boldsymbol{\varepsilon} \\ \mathbf{M} \end{Bmatrix} = \begin{bmatrix} \mathbf{A}^{-1} & -\mathbf{A}^{-1}\mathbf{B} \\ \mathbf{B}\mathbf{A}^{-1} & \mathbf{D} - \mathbf{B}\mathbf{A}^{-1}\mathbf{B} \end{bmatrix} \begin{Bmatrix} \mathbf{N} \\ \boldsymbol{\kappa} \end{Bmatrix} \tag{A.4}$$

Let $\mathbf{A}^* = \mathbf{A}^{-1}$, $\mathbf{B}^* = -\mathbf{A}^{-1}\mathbf{B}$, $\mathbf{H}^* = \mathbf{B}\mathbf{A}^{-1}$, $\mathbf{D}^* = \mathbf{D} - \mathbf{B}\mathbf{A}^{-1}\mathbf{B}$. Equation (4) can be expressed as

$$\begin{Bmatrix} \boldsymbol{\varepsilon} \\ \mathbf{M} \end{Bmatrix} = \begin{bmatrix} \mathbf{A}^* & \mathbf{B}^* \\ \mathbf{H}^* & \mathbf{D}^* \end{bmatrix} \begin{Bmatrix} \mathbf{N} \\ \boldsymbol{\kappa} \end{Bmatrix} \tag{A.5}$$

From Eq. (A.5), we have

$$\boldsymbol{\kappa} = -\mathbf{D}^{*-1}\mathbf{H}^*\mathbf{N} + \mathbf{D}^{*-1}\mathbf{M} \tag{A.6}$$

$$\boldsymbol{\varepsilon} = (\mathbf{A}^* - \mathbf{B}^*\mathbf{D}^{*-1}\mathbf{H}^*)\mathbf{N} + \mathbf{B}^*\mathbf{D}^{*-1}\mathbf{M} \tag{A.7}$$

According to Eqs. (4), (A.6) and (A.7) can be rewritten as

$$\begin{Bmatrix} \boldsymbol{\varepsilon} \\ \boldsymbol{\kappa} \end{Bmatrix} = \begin{bmatrix} \mathbf{A}^* - \mathbf{B}^*\mathbf{D}^{*-1}\mathbf{H}^* & \mathbf{B}^*\mathbf{D}^{*-1} \\ -\mathbf{D}^{*-1}\mathbf{H}^* & \mathbf{D}^{*-1} \end{bmatrix} \begin{Bmatrix} \mathbf{N} \\ \mathbf{M} \end{Bmatrix} \tag{A.8}$$

If there is no bending moment applied on the laminate, then we can obtain the expression of strain vector

$$\begin{aligned}\boldsymbol{\varepsilon} &= \left(\mathbf{A}^{*} - \mathbf{B}^{*}\mathbf{D}^{*-1}\mathbf{H}^{*}\right)\mathbf{N} \\ &= \left(\mathbf{A}^{-1} + \mathbf{A}^{-1}\mathbf{B}\left(\mathbf{D} - \mathbf{B}\mathbf{A}^{-1}\mathbf{B}\right)^{-1}\mathbf{B}\mathbf{A}^{-1}\right)\mathbf{N} = \mathbf{J}\mathbf{N}\end{aligned} \tag{A.9}$$

where

$$\begin{aligned}\boldsymbol{\varepsilon} &= \left\{\varepsilon_{11} \quad \varepsilon_{22} \quad \varepsilon_{33} \quad \varepsilon_{12}\right\}^{T}, \\ \mathbf{N} &= \left\{N_1 \quad N_2 \quad N_3 \quad N_{12}\right\}^{T},\end{aligned} \tag{A.10}$$

$$\mathbf{A} = \begin{bmatrix} A_{11} & A_{12} & A_{13} & A_{16} \\ A_{12} & A_{22} & A_{23} & A_{26} \\ A_{13} & A_{23} & A_{33} & A_{36} \\ A_{16} & A_{26} & A_{36} & A_{66} \end{bmatrix}, \quad \mathbf{B} = \begin{bmatrix} B_{11} & B_{12} & B_{13} & B_{16} \\ B_{12} & B_{22} & B_{23} & B_{26} \\ B_{13} & B_{23} & B_{33} & B_{36} \\ B_{16} & B_{26} & B_{36} & B_{66} \end{bmatrix}$$
$$\mathbf{D} = \begin{bmatrix} D_{11} & D_{12} & D_{13} & D_{16} \\ D_{12} & D_{22} & D_{23} & D_{26} \\ D_{13} & D_{23} & D_{33} & D_{36} \\ D_{16} & D_{26} & D_{36} & D_{66} \end{bmatrix}, \tag{A.11}$$

Appendix B

In Eqs. (42) and (43)

$$\begin{aligned} g_{30} = &-\gamma_{17} + m^2(\gamma_{18} + \gamma_{19})\frac{\gamma_{21}m^2 - \gamma_{23}}{\gamma_{22}m^2 + \gamma_{23}} \\ &- \left(\gamma_{29} + \gamma_{28}\frac{\gamma_{21}m^2 - \gamma_{23}}{\gamma_{22}m^2 + \gamma_{23}}\right)\frac{\gamma_{12}m^4}{\gamma_{22}m^2 + \gamma_{23}} \end{aligned} \tag{B.1}$$

$$\begin{aligned} g_{31} = &\, m^4\left[\gamma_{11} - \gamma_{12}\frac{\gamma_{21}m^2 - \gamma_{23}}{\gamma_{22}m^2 + \gamma_{23}}\right] \\ &+ 2m^2\pi\left[\gamma_{15} - \gamma_{14}\frac{\gamma_{21} - \gamma_{23}}{\gamma_{22} + \gamma_{23}}\right]\Phi \\ &+ 2\pi C_1\left[\gamma_{15} - \gamma_{14}\frac{\gamma_{21}m^2 - \gamma_{23}}{\gamma_{22}m^2 + \gamma_{23}}\right]\Phi \end{aligned} \tag{B.2}$$

$$\begin{aligned} g_{32} = &\, 2m^3\pi\left[\gamma_{15} - \gamma_{14}\frac{\gamma_{21}m^2 - \gamma_{23}}{\gamma_{22}m^2 + \gamma_{23}}\right] \\ &+ \frac{3}{4}\pi^2 C_2\gamma_{13}\Phi \end{aligned} \tag{B.3}$$

$$g_{33} = \frac{m^4\pi^2}{4}\gamma_{13} \tag{B.4}$$

$$g_q = \frac{2k_c bL^{5/2}}{\pi^3\bar{D}_{11}}\sin\frac{m}{2}\pi \tag{B.5}$$

$$g_i = -\frac{k_c\rho_0 L^{5/2}}{\pi^2 M E_0} \tag{B.6}$$

In Eqs. (B.2) and (B.3), C_1 and C_2 are dependent on the value of m. When $m = 1$, C_1 and C_2 are both equaled to 1. In other case, $C_1 = C_2 = 0$.

References

Abrate, S.: Impact Engineering of Composite Structures. Springer, Berlin (2011)

Bayat, M.R., Rahmani, O., Mashhadi, M.M.: Nonlinear low-velocity impact analysis of functionally graded nanotube-reinforced composite cylindrical shells in thermal environments. Polym. Compos. **39**, 730–745 (2018)

Chen, Y.J., Scarpa, F., Farrow, I.R., Liu, Y.J., Leng, J.S.: Composite flexible skin with large negative Poisson's ratio range: numerical and experimental analysis. Smart Mater. Struct. **22**, 045005 (2013)

Clarke, J.F., Duckett, R.A., Hine, P.J., Hutchinson, I.J., Ward, I.M.: Negative Poisson's ratios in angle-ply laminates: theory and experiment. Composites **25**, 863–868 (1994)

Dai, H.-L., Yan, X., Jiang, H.-J.: Investigation on thermomechanical behavior of a HSLA steel circular plate under impact load. Int. J. Mech. Mater. Des. **10**, 411–420 (2014)

Ebrahimi, F., Habibi, S.: Low-velocity impact response of laminated FG-CNT reinforced composite plates in thermal environment. Adv. Nano Res. **5**, 69–97 (2017)

Evans, K.E., Nkansah, M.A., Hutchinson, I.J., Rogers, S.C.: Molecular network design. Nature **353**, 124 (1991)

Fan, Y., Wang, H.: The effects of matrix cracks on the nonlinear bending and thermal postbuckling of shear deformable laminated beams containing carbon nanotube reinforced composite layers and piezoelectric fiber reinforced composite layers. Compos. B **106**, 28–41 (2016)

Fan, Y., Wang, H.: Nonlinear low-velocity impact analysis of matrix cracked hybrid laminated plates containing CNTRC layers resting on visco-Pasternak foundation. Compos. Part B **117**, 9–19 (2017a)

Fan, Y., Wang, H.: Nonlinear low-velocity impact on damped and matrix-cracked hybrid laminated beams containing carbon nanotube reinforced composite layers. Nonlinear Dyn. **89**, 1863–1876 (2017b)

Fan, Y., Xiang, Y., Shen, H.-S., Wang, H.: Low-velocity impact response of FG-GRC laminated beams resting on visco-elastic foundations. Int. J. Mech. Sci. **141**, 117–126 (2018a)

Fan, Y., Xiang, Y., Shen, H.-S., Hui, D.: Nonlinear low-velocity impact response of FG-GRC laminated plates resting on visco-elastic foundations. Compos. B **144**, 184–194 (2018b)

Fan, Y., Xiang, Y., Shen, H.-S.: Temperature-dependent mechanical properties of graphene/Cu nanocomposites

with in-plane negative Poisson's ratios. Research **2020**, 5618021 (2020)
González, E.V., Maimí, P., Camanho, P.P., Turon, A., Mayugo, J.A.: Simulation of drop-weight impact and compression after impact tests on composite laminates. Compos. Struct. **94**(11), 3364–3378 (2012)
Greszczuk, L.B.: Damage in composite materials due to low velocity impact. In: Zukas, J.A., et al. (eds.) Impact Dynamics. Wiley, New York (1982)
Han, Y., Elliott, J.: Molecular dynamics simulations of the elastic properties of polymer/carbon nanotube composites. Comput. Mater. Sci. **39**, 315–323 (2007)
Harkati, E.H., Bezazi, A., Scarpa, F., Alderson, K., Alderson, A.: Modelling the influence of the orientation and fibre reinforcement on the negative Poisson's ratio in composite laminates. Phys. Stat. Sol. **244**, 883–892 (2007)
Heydari-Meybodi, M., Saber-Samandari, S., Sadighi, M.: An experimental study on low-velocity impact response of nanocomposite beams reinforced with nanoclay. Compos. Sci. Technol. **133**, 70–78 (2016)
Heyliger, P.R., Reddy, J.N.: A higher-order beam finite element for bending and vibration problems. J. Sound Vib. **126**, 309–326 (1988)
Hill C.B., Wang Y., Zhupanska O.I.: Effects of carbon nanotube buckypaper layers on the electrical and impact response of IM7/977-3 composite laminates. American Society for Composites 27th Annual Technical Conference, Arlington, TX. (2012)
Hill C.B., Wang Y., Zhupanska O.I.: Impact response of CFRP laminates with CNT buckypaper layers. In: 54th AIAA/ASME/ASCE/AHS/ASC Structures, Structural Dynamics and Materials Conference, Boston, MA (2013). https://doi.org/10.2514/6.2013-1617
Hou, X., Hu, H., Silberschmidt, V.: A novel concept to develop composite structures with isotropic negative Poisson's ratio: effects of random. Compos. Sci. Technol. **72**(15), 1848–1854 (2012)
Jam, J.E., Kiani, Y.: Low velocity impact response of functionally graded carbon nanotube reinforced composite beams in thermal environment. Compos. Struct. **132**, 35–43 (2015)
Kwon, H., Bradbury, R.C., Leparoux, M.: Fabrication of functionally graded carbon nanotube-reinforced aluminum matrix composite. Adv. Eng. Mater. **13**, 325–329 (2011)
Malekzadeh, P., Dehbozorgi, M.: Low velocity impact analysis of functionally graded carbon nanotubes reinforced composite skew plates. Compos. Struct. **140**, 728–748 (2016)
Mir, M., Ali, M.N., Sami, J., Ansari, U.: Review of mechanics and applications of auxetic structures. Adv. Mater. Sci. Eng. **2014**, 753496 (2014)
Mittal, R.K., Khalili, M.R.: Analysis of impact of a moving body on an orthotropic elastic plate. AIAA J. **32**, 850–856 (1994)
Olsson, R., Donadon, V.M., Falzon, G.B.: Delamination threshold load for dynamic impact on plates. Int. J. Solids Struct. **43**, 31241–33141 (2006)
Pham, D.C., Lua, J., Sun, H., Zhang, D.: A three-dimensional progressive damage model for drop-weight impact and compression after impact. J. Compos. Mater. **54**(4), 449–462 (2020)
Rilo, N.F., Ferreira, L.M.S.: Experimental study of low-velocity impacts on glass-epoxy laminated plates. Int. J. Mech. Mater. Des. **4**, 291–300 (2008)
Salami, S.J.: Low velocity impact response of sandwich beams with soft cores and carbon nanotube reinforced face sheets based on Extended High Order Sandwich Panel Theory. Aerosp. Sci. Technol. **66**, 165–176 (2017)
Shen, H.-S.: Nonlinear bending of functionally graded carbon nanotube reinforced composite plates in thermal environments. Compos. Struct. **91**, 9–19 (2009)
Shen, H.-S., Zhang, C.-L.: Thermal buckling and postbuckling behavior of functionally graded carbon nanotube-reinforced composite plates. Mater. Des. **31**, 3403–3411 (2010)
Shen, H.-S., Li, C., Reddy, J.N.: Large amplitude vibration of FG-CNTRC laminated cylindrical shells with negative Poisson's ratio. Comput. Methods Appl. Mech. Eng. **36**, 112727 (2020a)
Shen, H.-S., Huang, X.-H., Yang, J.: Nonlinear bending of temperature-dependent FG-CNTRC laminated plates with negative Poisson's ratio. Mech. Adv. Mater. Struct. (2020b). https://doi.org/10.1080/15376494.2020.1716412
Song, Z.G., He, X., Liew, K.M.: Dynamic responses of aerothermoelastic functionally graded CNT reinforced composite panels in supersonic airflow subjected to low-velocity impact. Compos. B **149**, 99–109 (2018)
Sun, C.T., Chen, J.K.: On the impact of initially stressed composite laminates. J. Compos. Mater. **19**, 490 (1985)
Sveklo, V.A.: Hertz problem of compression of anisotropic bodies. J. Appl. Math. Mech. **38**, 1023–1027 (1974)
Swanson, S.R.: Contact deformation and stress in orthotropic plates. Compos. A **36**, 1421–1429 (2005)
Tan, K.T., Watanabe, N., Iwahori, Y.: Impact damage resistance, response, and mechanisms of laminated composites reinforced by through-thickness stitching. Int. J. Damage Mech. **21**(1), 51–80 (2012)
Takakura, A., Beppu, K., Nishihara, T., Fukui, A., Kozeki, T., Namazu, T.: Strength of carbon nanotubes depends on their chemical structures. Nat. Commun. **10**, 3040 (2019)
Turner, J.R.: Contact on a transversely isotropic half-space, or between two transversely isotropic bodie. Int. J. Solids Struct. **16**, 409–419 (1979)
Wang, Z.-X., Xu, J., Qiao, P.: Nonlinear low-velocity impact analysis of temperature-dependent nanotube-reinforced composite plates. Compos. Struct. **108**, 423–434 (2014)
Yang, J., Huang, X.-H., Shen, H.-S.: Nonlinear flexural behavior of temperature-dependent FG-CNTRC laminated beams with negative Poisson's ratio resting on the Pasternak foundation. Eng. Struct. **207**, 110250 (2020a)
Yang, J., Huang, X.-H., Shen, H.-S.: Nonlinear vibration of temperature-dependent FG-CNTRC laminated plates with negative Poisson's ratio. Thin Walled Struct. **148**, 106514 (2020b)
Zarei, H., Fallah, M., Bisadi, H., Daneshmehr, A., Minak, G.: Multiple impact response of temperature-dependent carbon nanotube-reinforced composite (CNTRC) plates with general boundary conditions. Compos. B **113**, 206–217 (2017)